

Optical Biosensing of Multiple Disease Markers in a Photonic-Band-Gap Lab-on-a-Chip: A Conceptual Paradigm

Abdullah Al-Rashid* and Sajeev John†

Department of Physics, University of Toronto, 60 Saint George Street, Toronto, Ontario M5S 1A7, Canada
(Received 23 October 2014; revised manuscript received 24 January 2015; published 2 March 2015)

A conceptual paradigm for multiparametric optical biosensing in a lab-on-a-chip, using the cascaded transmission of light through a photonic crystal that contains microfluidic channels and is embedded in a glass slide, is demonstrated. Accurate detection of multiple disease-identifying biomarkers is facilitated by the interaction of surface and photonic-band-gap waveguide modes. Through finite-difference time-domain simulations, levels of light transmission through the device are shown to be simultaneously responsive to analyte bindings and layer thicknesses at different locations along a single optical transmission path through the photonic crystal. Our multiparametric biosensing mechanism supersedes traditional single-resonance-shift-based biosensing and provides a more detailed spectral fingerprint of various diseases or various stages of a given disease. Moreover, the spectral line shape due to the engineered optical modes can logically discriminate between different concentrations of several analytes flowing through the microfluidic channels. The simultaneous detection and differentiation of (combinations of) distinct analytes using a single measurement on one device offers a paradigm for optical biosensing.

DOI: 10.1103/PhysRevApplied.3.034001

I. INTRODUCTION

Lab-on-a-chip (LOC) optical biosensing offers a rapid and simple means for medical diagnostics. The ultimate goal is to detect and monitor early-stage disease markers from body tissue and fluid samples almost instantly and *in situ* by using a millimeter- to centimeter-scale optical chip—without recourse to time-consuming and expensive external laboratory testing. Such a biosensor is functionalized by the attachment of antibodies or DNA aptamers [1] to interior surfaces in different regions of the optical chip that can bind predetermined disease-identifying proteins or other biological molecules, leading to a detectable change in the optical-resonance characteristics of the chip. In this article, we demonstrate, by using a simplified paradigm, that many of the ultimate features of the LOC optical biosensor can be realized by using a thin-film, photonic-band-gap (PBG) material containing microfluidic channels as the active region of the chip. The distinctive features include the realization of high sensitivity and a low limit of detection. Also, the PBG material provides a “clean slate” in which desired optical resonances are well separated in frequency from spurious resonances that can clutter the detected signal with unwanted noise. Most significantly, our proposed LOC uses extended optical modes that overlap a large volume of the fluid sample and provides detailed spectral fingerprints that can distinguish between different concentrations of multiple disease markers in a

single measurement. This proposal offers considerably greater functionality than conventional biosensors studied previously.

Photonic crystals (PCs) [2,3] are dielectric materials engineered with periodic variations of about half the wavelength of light. Most notably, certain PCs completely inhibit the propagation of light through them over a range of frequencies known as the *photonic band gap* (PBG). PBGs offer “blank slates” for engineering optical modes within defects surrounded by the bulk PC [4]. These *defect modes* concentrate light spatially within and near the defect regions. As light may not propagate through the PC material surrounding the defect due to the existence of the PBG, defect modes can confine light in either the high- or low-refractive-index regions of the optical microstructure. It is quite common for such states to exist in lines of altered unit cells in a PC, giving rise to a waveguide effect due to the associated *line-defect modes*. Surfaces truncating an infinite PC also give rise to guided *surface modes* [5]. The PBG provides an opportunity for optical sensing, in which high-quality-factor modes can have field energies concentrated in the low-refractive-index regions, where the *analyte* to be detected is likely to reside. PBG-based sensing thereby enables very high sensitivity without sacrificing a low limit of detection. The former property requires strong optical overlap of the electromagnetic field with the analyte, whereas the latter property traditionally requires a high quality factor of the field mode. These two properties are often in opposition in conventional biosensors that do not utilize a PBG.

In our biosensing mechanism, the weak coupling between an interior PBG waveguide and nearby surface

*abdullah.alrashid@utoronto.ca

†john@physics.utoronto.ca; <http://www.physics.utoronto.ca/~john/>

modes provides a detailed spectral fingerprint of the presence of multiple analytes. This situation occurs not only from frequency shifts of optical resonances due to analyte binding, but as a result of other features of the spectral signature arising from changes in coupling between the optical-resonance modes. An important aspect of our biosensor is that it utilizes extended (guided) optical-resonance modes rather than point-localized modes [6]. Using a mousetrap analogy, this aspect makes it easier for the “mouse” (i.e., analyte) to find the “trap” (i.e., binding sites) by spreading it over a larger region, thereby reducing the time required for detection.

Mathematically, optical modes in a PC are described by *Maxwell’s wave equation* [7]:

$$\vec{\nabla} \times \{ \vec{\nabla} \times [\epsilon^{-1}(\mathbf{r}) \cdot \mathbf{H}_{j,\mathbf{k}}(\mathbf{r})] \} = \left[\frac{\omega_j(\mathbf{k})}{c} \right]^2 \mathbf{H}_{j,\mathbf{k}}(\mathbf{r}). \quad (1)$$

The magnetic-field eigenfunction $\mathbf{H}_{j,\mathbf{k}}(\mathbf{r})$ of the wave equation (1) represents the spatial field distribution for the j th mode of the PC—corresponding to (angular) frequency $\omega_j(\mathbf{k})$ —at a given wave vector \mathbf{k} . A similar, but slightly different, equation applies for the electric fields $\mathbf{E}_{j,\mathbf{k}}(\mathbf{r})$. In accordance with an orthogonality condition satisfied by these eigenfunctions, the fields for the lower-frequency modes tend to be confined to higher-refractive-index regions. For clarity, we refer to such modes as “skeleton modes” of the biosensor. The “skeleton” consists of a high-index solid, such as silicon, containing a periodic array of microfluidic channels. Accordingly, we refer to optical modes concentrated mainly in the lower-index modes as the “fluidic modes.” In air-dielectric PCs, modes analogous to the foregoing are often referred to as the “dielectric modes” and the “air modes” [7].

PC-based optical biosensors without a PBG are utilized by many researchers. Light concentration—in the region of the analyte to be detected—has been identified as vital for effective sensitivity. PC-based biosensors often incorporate defect structures [6,8–10] due to their ability to concentrate light in regions where periodicity is broken. However, neither the interaction of multiple defect modes nor the use of a complete PBG to eliminate spurious optical modes has been fully explored.

Traditional biosensors are characterized by two key *performance metrics*: (i) *Sensitivity* is the change in output signal (e.g., transmission resonance frequency, transmission levels at resonance, etc.) resulting from an infinitesimal change in the analyte (e.g., binding thickness). (ii) *Limit of detection* is the minimum amount of analyte variation required to detect an output signal change. In traditional biosensors that confine light by total internal reflection, these two metrics are usually opposed to each other. High sensitivity requires the optical field of a resonance to have a strong evanescent component in the lower-index region where the analyte resides.

Unfortunately, this strong evanescence is often accompanied by a lowering of the quality factor of the optical resonance [11].

A number of optical biosensors are now commercially available. Many of these sensors employ surface plasmon resonance (SPR) [12]. Among the drawbacks of SPR sensors, the lossy nature of the metallic surface as well as the need for complicated light-coupling mechanisms—such as prisms—are the most notable. Numerous grating and waveguide-based sensors have also been previously proposed. Our design enhances the mechanism of waveguide biosensors [9], grating-based sensors [13], and grating-coupled waveguide sensors (e.g., optical waveguide light-mode sensors) [14–16]. We employ a dual-grating arrangement for light coupling into and out of a waveguide. In our design, both surface gratings, as well as the interior waveguide, offer analyte-binding sites, leading to multiparametric detection based on a single transmission spectrum measurement.

In a conventional biosensor detecting thin-layer analytes, the frequency shift of transmission or reflection resonances is the indicator of analyte binding. In a PC structure with multiple modes, we consider the m th mode of the PC-based biosensor to shift slightly in (angular) frequency from ω_m to ω'_m due to a “small” change δt in analyte binding, i.e., thickness changes from t to $(t + \delta t)$. The corresponding frequency change $\delta\omega_m = \omega'_m - \omega_m$ defines the sensitivity S_m of the m th mode of the system for resonance shifts (an additional transmission-level sensitivity is described later):

$$S_m \equiv \frac{\delta\omega_m}{\delta t} = \omega_m \mathfrak{F}_m. \quad (2)$$

In Eq. (2), \mathfrak{F}_m is a measure of the optical field concentration at the binding surface for the incremental analyte layer of thickness δt . A detailed prescription for calculating \mathfrak{F}_m is given in Appendix A. We note here that the quantity \mathfrak{F}_m has the dimension of inverse length and may be physically thought of as the optical field concentration per unit length of analyte increment around the analyte-binding surface. Consequently, sensitivity has units of the frequency shift per unit of the analyte-thickness change.

The limit of detection $t_m^{(\text{lim})}$ of the m th spectral resonance is defined in terms of its *quality factor* Q_m as

$$t_m^{(\text{lim})} \equiv \frac{\eta}{\mathfrak{F}_m Q_m}. \quad (3)$$

For the limit of detection defined by Eq. (3), the quantity η is a dimensionless number, of the order of unity, corresponding to the minimum resolvable separation between two adjacent resonance peaks in a spectrometer used for the biosensing task. As per the definition of \mathfrak{F}_m [cf. Eq. (A3) in Appendix A], the limit of detection has the dimension of the analyte thickness.

While the traditional biosensing mechanism defined by the above metrics considers only individual resonance shifts, our proposed multiparametric biosensor also exploits the change in coupling between modes of a PC induced by different analyte bindings. This difference gives rise to changes in light-transmission peak levels—in addition to frequency shifts—in response to changes to analyte-layer thickness. This change provides a more detailed spectral fingerprint for multiple disease markers in a sample.

Some previous liquid-infiltrated PC biosensors rely upon refractive-index changes to the entire liquid fraction of the device [11,17]. In contrast, our biosensor detects thin-layer analytes attached to designated binding sites in the PC. The former approach has very significant limitations. For example, in a sample of blood plasma, it is possible that different proportions of different protein components of the mixture can lead to the same value of refractive index for the fluid. In order to detect specific substances within a very mixed sample like blood plasma, it will be essential to isolate them. Our multiparametric PC biosensor detects analytes through binding (which can also be described as isolation or immobilization) based on *biorecognition*. The biorecognition occurs via the binding of complementary biological molecules, such as antibody-antigen binding, or DNA aptamer-protein binding [1,18]. Recognition agents are placed at specific locations in the PC, where the arrival—and subsequent binding—of complementary disease markers alters optical resonances as well as couplings between optical modes.

Structurally, the repetitive geometry of the PC provides a convenient set of extended biorecognition sites spread over the many PC unit cells, allowing for a broad “net” to capture disease markers. Additionally, PCs can be designed in a variety of ways to admit large flow channels—both at the surface and within the interior of the chip. Fluid flow through PCs for the purpose of sensing is demonstrated in previous literature [19,20].

The PBG plays a pivotal role in our design, providing a blank slate for engineering the optical modes tailored specifically towards the biosensing task at hand. A complete omnidirectional PBG—as opposed to an incomplete stop gap—offers a greater robustness and *signal-to-noise ratio* for the sensor. Once the biosensing modes are generated to lie within the PBG, there is a sufficient *free spectral range* available for these modes to be “uncluttered” in frequency space due to the absence of other spurious modes accessible by improper beam collimation, disorder-induced scattering, or finite-size effects.

II. DESIGN OF SURFACE AND LINE-DEFECT MODES

We consider a two-dimensional (2D) PC LOC to illustrate our multiparametric biosensing paradigm. The square-lattice PC unit cell (Fig. 1) is formed by the immersion of a square dielectric block of refractive index

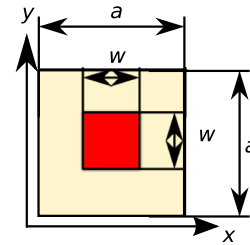


FIG. 1. Unit cell for the underlying PC architecture used for the proposed design. Dark shading indicates solid, high-refractive-index material, and light shading indicates fluid background. The choice of $w/a = 0.40$ provides an optimum 2D PBG.

$n = 3.4$ ($\epsilon = 11.56$) in a fluid matrix of $n = 1.35$ ($\epsilon = 1.8225$). The unit cell shown is an $a \times a$ square with a $w \times w$ square dielectric block at the center. We choose $w/a = 0.40$ to optimize the 2D PBG of the PC for light with the electric field polarized out of the plane (i.e., in the z direction). The system has a complete PBG for $0.263 \leq (\omega a)/(2\pi c) \leq 0.326$, i.e., an approximately 21.5% band gap to center frequency ratio.

The active region of our chip [Fig. 2(a)] starts with a $2 \times (2l + 1)$ supercell, consisting of two unit cells in the x direction and $(2l + 1)$ unit cells in the y direction. We identify, below, the optimal value of l for our biosensing application. The chip is encased in glass ($n = 1.5$, $\epsilon = 2.25$), forming a superstrate above and a substrate below it in the y direction. The structure is periodically repeated in the x direction.

We now modify the basic PC, such that the resulting chip admits a central waveguide mode and two surface modes, which can all be excited by an external plane wave impinging on the chip along the y direction, normal to its surface. We also require that the surface and waveguide modes are nearly in resonance with each other. Detailed geometric modifications are shown in Fig. 2(a). Along the y center of the finite-thickness PC, we introduce a *line defect* consisting of smaller dielectric blocks of alternating side lengths w_{wg} and $(w_{\text{wg}} + \delta w_{\text{wg}})$. This structure forms a single-mode waveguide. There are l unit cells of PC above and below this central line defect. In the dielectric blocks at the top and the bottom of the chip (adjacent to the glass superstrate-substrate structure), we increase the side length of alternate squares (in the x direction) to $(w + \delta w_{\text{sg}})$. This structure serves as a grating coupler for incident and exiting light. In order to generate surface modes in the grating region, we extend the glass superstrate-substrate structure to encroach into the PC unit cells lying adjacent to them by a distance of $(\tau \times a)$, where τ is the *surface truncation parameter* satisfying the requirement $\tau \in [0, 1)$ [cf. Fig. 2(b)]. It is important to note that not all values of τ ensure the existence of a surface mode for the grating coupler, and the choice of τ provides a limited range of freedom for tailoring these surface-mode frequencies. There are now $(l - \tau)$ unit cells of PC material above and below the central line-defect region.

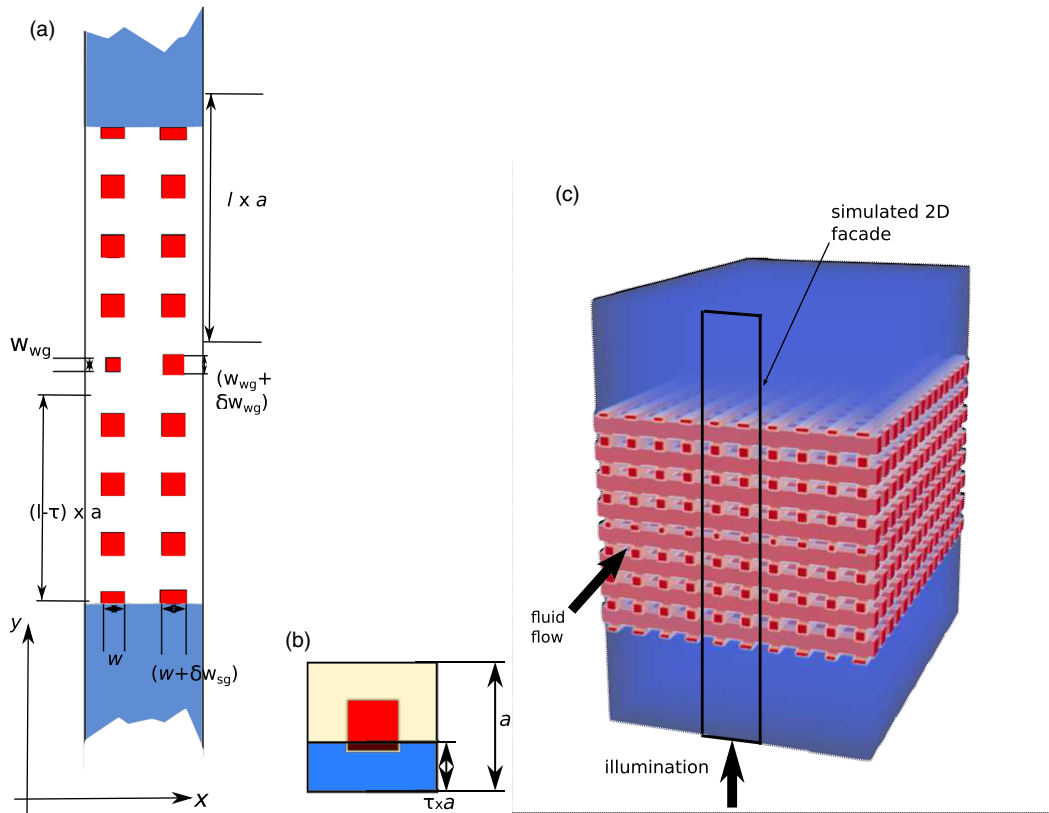


FIG. 2. Geometry for the proposed structure. (a) A 2D prototype LOC biosensor: The 2D structure is based on the PC unit cell in Fig. 1. The structure is periodic along the x direction and truncated by the infinite glass superstrate-substrate structure along the y direction. In our ideal chip, we choose $w/a = 0.40$, $w_{wg}/a = 0.25$, $\delta w_{wg}/a = 0.10$, and $\delta w_{sg}/a = 0.05$. (b) Illustration of the concept of the truncation parameter τ at the terminations: The parameter τ denotes the proportion of the PC unit cell intruded into by the encroaching glass material. Alignment of central waveguide and surface modes is achieved by using $\tau = 0.50$. (c) An artist's rendition of a LOC device in 3D: The final device is potentially based on a simplified woodpile architecture embedded in glass. The chip is illuminated from below. The 2D prototype is in rough correspondence to a facade of this 3D chip.

Our 2D model is a prototype for essential design principles and the multiparametric biosensing paradigm. In a real 3D LOC biosensor, the solid square regions of the 2D PC [Fig. 2(a)] can represent square-log cross sections of a 3D simplified woodpile PBG material [cf. Fig. 2(c)]. These logs extend in the z direction and are separated by orthogonal logs extending in the x direction and periodically arrayed in the z direction. This 3D architecture is structurally stable and contains a connected network of microfluidic channels. In 3D, the line-defect mode becomes a planar guided mode. Our 2D model illustrates the design and biosensing principle of the realistic 3D LOC using a simplified geometry. In our simplified model, we assume a perfect antireflection coating at the exterior glass surface to air. We consider only *TM-polarized* light, for which the electric field lies along the z direction, perpendicular to the plane of the 2D PC.

Our LOC biosensor is designed to operate in *optical transmission mode*, whereby detailed spectral signatures of multiple disease markers are displayed through light transmitted from the substrate to the superstrate of the chip. This display requires a sequence of energy and momentum conservation steps for the incident photons.

External light coupling into surface modes requires specific design considerations. On a photonic band diagram, surface modes appear *below the light line* of the encasing superstrate-substrate structure [5]. To compensate for this, additional transverse momentum must be supplied (by a prism or surface grating) to photons incident externally to couple to the propagating surface-localized modes. A doubling of the spatial period of a structure by a surface grating halves the period in \mathbf{k} -space of the band diagram, resulting in a *band-folding effect*, in which surface-mode bands are folded back onto the Γ point ($\mathbf{k} = \mathbf{0}$). This folding is achieved by a perturbation of δw_{sg} to the dielectric blocks lying at the surface of the truncated PC [Fig. 2(a)]. The small period-doubling perturbation changes the mode frequencies very slightly but folds the surface-mode bands to lie *above* the light line, making them accessible by normally incident light [cf. Fig. 3(a)].

Given the finite dwell time of incident photons in the surfaces and central waveguide (as defined by their respective quality factors), an exact frequency match between these modes is not required for a photon to

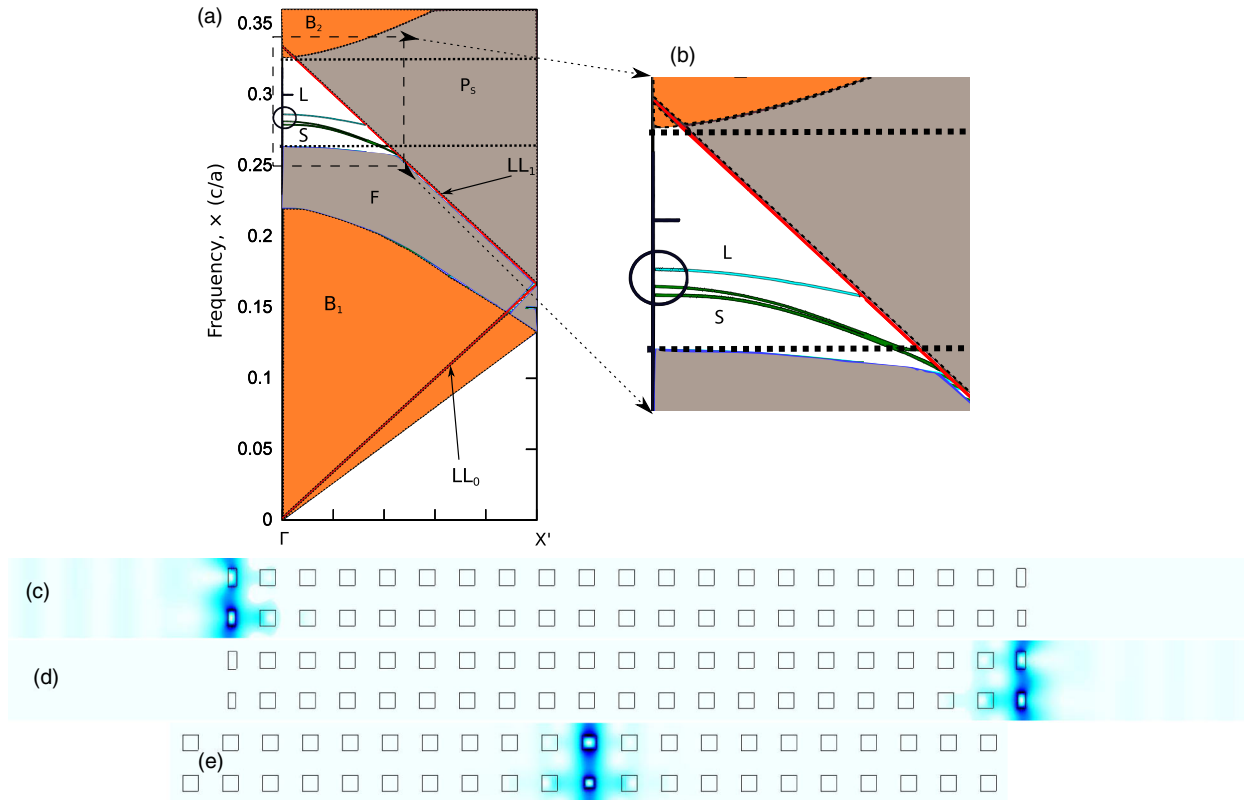


FIG. 3. Alignment of surface and line-defect modes. (a) Combined band diagram for the folded surface and line-defect bands: The folded outline of region B_1 forms the skeleton modes of the PC in Fig. 1. The outline of B_2 denotes fluidic modes. Surface bands S and line-defect bands L lie within the complete PBG (dashed horizontal lines). The *light line* LL_0 for glass encasing the LOC is folded to form LL_1 . Folded S bands lie *above* the unfolded light line LL_0 , making them accessible by light incident from the glass. [Note: Region F constitutes modes that correspond to the *finite-size effect* due to the supercells [cf. (c)–(e)] used for S and L calculations (modes of adjacent unit cells in supercells interact to form a continuum of states between the complete PBG and the Γ - X stop gap). P_S is the region of propagating modes in the glass superstrate-substrate structure (which are *not* modes of the PC at all).] (b) Magnified view of surface and line-defect modes: The S and L bands are nearly aligned at the Γ point as emphasized within the circle. (c),(d) Surface-mode field intensities depicted over the S_{PWEM} supercell: Upper and lower surface modes are degenerate by symmetry. The geometry is similar to the one in Fig. 2(a) but missing the central line defect. (e) Line-defect-mode field intensities depicted over the L_{PWEM} supercell: The line-defect-mode calculations do not involve embedding of the PC in the glass superstrate-substrate structure.

evanescently couple from the surface to the central modes by tunneling through the PBG. Nevertheless, energy conservation requires that their frequency mismatch not be large compared to their individual resonance linewidths.

To fine-tune the central waveguide spectrum, a period-doubling perturbation δw_{wg} is also introduced into the waveguide line defect to alternating defect blocks [Fig. 2(a)]. This perturbation enables finer alignment of the surface and line-defect modes in the ω - \mathbf{k} space than is possible by exploring changes to w_{wg} alone. Details of the alignment of surface and line-defect modes at the Γ point on a band diagram are shown in Fig. 3(b).

Band diagrams for the surface and line-defect modes are computed by using the *plane-wave expansion method* (PWEM), implemented by the freely available software MIT PHOTONIC BANDS [21]. For all PWEM calculations, a spatial resolution of 64 mesh points per unit cell is employed in each direction, resulting in the same number

of plane waves being used to calculate the field distributions. A search over the geometric parameters τ , δw_{sg} , w_{wg} , and δw_{wg} is performed to find suitable surface and line-defect-mode frequencies that are almost coincident at the Γ point ($\mathbf{k} = \mathbf{0}$) of the band diagram. As seen in Figs. 3(a) and 3(b), the doubly degenerate surface modes (the top and bottom surface modes are degenerate by mirror symmetry) are close but not exactly coincident with the line-defect mode at the Γ point. This small *free spectral range* between the surface and line-defect frequencies plays a vital role in the functionality of our biosensor. It allows for conventional frequency-shift biosensing by the surface and line-defect modes individually. More significantly, the analyte-binding-dependent frequency overlap between the resonance peaks related to surface and line-defect modes provides a variable fingerprint in both the spectral position and transmitted intensity for multiple disease markers.

For a PC with lattice constant a , consisting of square dielectric blocks of $\epsilon = 11.56$ ($n = 3.4$) and side length $w/a = 0.40$ immersed in a fluid background of $\epsilon = 1.8225$ ($n = 1.35$), the following values of the other geometric parameters are found to reasonably align the surface and line-defect modes: $\tau = 0.50$, $\delta w_{sg}/a = 0.05$, $w_{wg}/a = 0.25$, and $\delta w_{wg}/a = 0.10$ [Figs. 3(a) and 3(b)]. Surface modes localized at the top and bottom surfaces of the S_{PWEM} supercell [Figs. 3(c) and 3(d)] are degenerate and are numerically calculated to have normalized frequencies $(\omega a)/(2\pi c) = 0.281$ and 0.282 at the Γ point. The very slight splitting of the calculated surface-mode frequencies is due to a weak coupling between the modes. The $|\mathbf{H}_{m,\mathbf{k}=0}(\mathbf{r})|^2$ field patterns for these calculated modes are shown in Figs. 3(c) and 3(d). The central waveguide mode with frequency $(\omega a)/(2\pi c) = 0.286$ at the Γ point has the mode pattern depicted in Fig. 3(e), which also shows the L_{PWEM} supercell used to calculate the modes. The approximate alignment at the Γ point of the surface and line-defect modes is seen in Fig. 3(b). These modes, obtained from supercell band structure calculations, provide an interpretative tool for our finite-difference time-domain (FDTD) simulation results on the actual finite-size chip.

III. SIMULATION OF OPTICAL TRANSMISSION

FDTD simulations of total optical transmission through the PC chip are performed by using MEEP [22]. Normally incident plane waves illuminate the symmetric chip consisting of a central line defect separated by $(l - 1)$ unit cells of PC from τ -truncated surfaces both above and below [cf. Fig. 2(a), for which $\tau = 0.50$ and $l = 4$]. The FDTD light source is embedded in the glass substrate below the chip. *Bloch-periodic boundary conditions* are imposed along the x boundaries and *perfectly matched layer absorbers* are placed at the y extremities of the geometry.

The results of FDTD simulation with various spatial resolutions are an indicator of the response of the biosensor to various degrees of fabrication imperfection (cf. Appendix C). That is to say, random structural variations in a real biosensor on scales smaller than our FDTD mesh spacing have a negligible effect on the predicted transmission spectral fingerprint. Two values are used for the spatial resolution of the FDTD calculations. Both 40 and 80 mesh points per lattice constant are implemented, and their results compared (with the majority of the discussion relegated to Appendix C). Analyte material is considered to have a refractive index $n = 1.45$ ($\epsilon = 2.1025$). Four different analyte thicknesses are considered: $t/a \in \{0.025, 0.050, 0.075, 0.100\}$. These analyte-thickness increments correspond to a single mesh step for the simulation using 40 mesh points per lattice period.

Three primary sites are considered for analyte binding on the interior surfaces of the microfluidic chip, namely, the

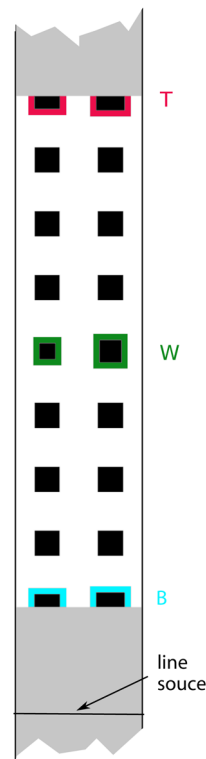


FIG. 4. The three primary sites for analyte binding in the biosensor. These are labeled as W (central line-defect waveguide), B (bottom surface grating), and T (top surface grating). The line source is used to illuminate the device during the FDTD calculations.

top and bottom surface gratings, as well as the waveguide line defect—represented in Fig. 4 by red, green, and blue outlines, respectively. We label these sites as W (for waveguide), T (for top surface grating), and B (for bottom surface grating). Various combinations of analyte binding, corresponding to three distinct disease markers, are studied, revealing a variety of different spectral signatures in transmission. In particular, a total of seven combinations of analyte binding are possible with binding in at least one of the three binding sites.

For simplicity, we ignore the thickness of the biorecognition layer and implicitly assume that it has a refractive index equal to that of the analyte. In our model, analyte binding simply enhances the thickness of the thin-film layer around the binding sites.

IV. SPECTRAL FINGERPRINTS OF ANALYTE BINDING

A. Conventional resonance-shift biosensing

We begin by recapturing the behavior of a traditional optical biosensor based on individual surface or line-defect resonance modes using two simplified device designs. The first, referred to as the *S chip*, involves surface modes only.

Here, we use the geometry shown in Fig. 2(a) with $l = 4$ and choose ($w_{\text{wg}} = w$, $\delta w_{\text{wg}} = 0$) to eliminate the central waveguide completely. We retain $\delta w_{\text{sg}}/a = 0.05$ and $\tau = 0.50$, so that the structure admits surface modes. The second, referred to as the *L chip*, involves the central line-defect waveguide modes only. Here, we choose $\delta w_{\text{sg}} = 0$ and $\tau = 0$ to eliminate surface modes completely while retaining the waveguide line defect with $w_{\text{wg}}/a = 0.25$ and $\delta w_{\text{wg}} = 0.10$. The effects of analyte binding on the transmission spectrum for the S chip and the L chip are shown in Fig. 5 based on a spatial resolution of 80 mesh points per unit of periodicity for the FDTD calculations.

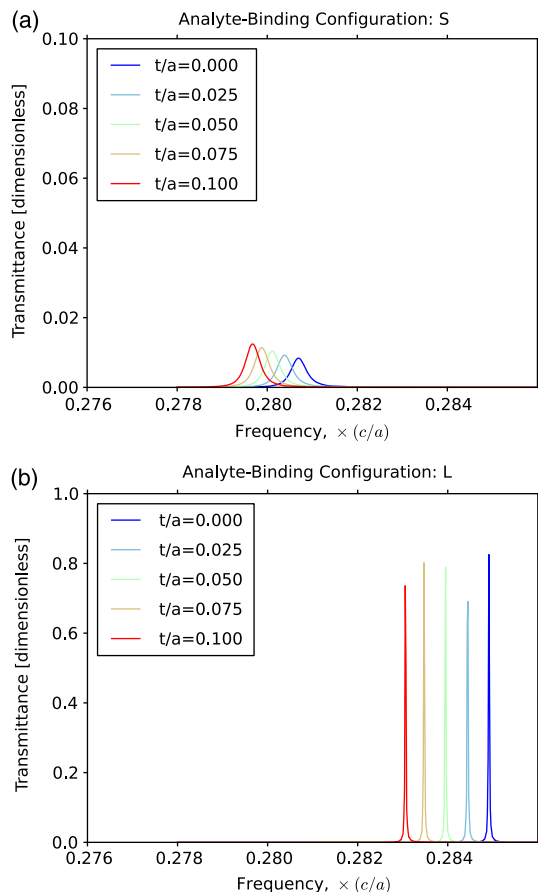


FIG. 5. Effects of analyte binding on the proposed lab-on-a-chip with surface modes or line-defect modes only. (a) Transmission spectra for analyte binding to both surface gratings for a structure admitting surface modes but no line-defect modes (S chip): This chip is a traditional resonance-shift biosensor with very low transmission levels. The y scale for this plot has been expanded to show peak details. (b) Transmission spectra for analyte binding to waveguide blocks for a structure admitting line-defect modes but no surface modes (L chip): This chip is a traditional resonance-shift biosensor for the line-defect modes. [Note: The absence of a sufficient frequency resolution for plots in (b), as indicated by the variable peak levels, is a negligible issue. Here, we seek only to demonstrate that spectral lines redshift due to analyte binding.]

For the S chip [Fig. 5(a)], the total transmission coefficient is less than 2% for a thick ($l = 4$) chip. With increments to the analyte-layer thickness around the surface-grating blocks, the weak transmission resonance shifts to lower frequencies. Clearly, the S chip acts like a conventional biosensor—with very weak transmission due to the long tunneling distance of photons through the PBG from the bottom to the top surface modes. The confined surface modes decay exponentially into the PC material, wherein the “tails” of their evanescent fields overlap, establishing a very weak coupling between two degenerate modes. However, the strength of the evanescent coupling is small compared to the resonance linewidth of each surface mode. As a result, only a single transmission peak can be resolved, despite the presence of two coupled resonances (cf. Appendix B).

The S-chip response indicates that a separation of seven unit cells of PC material between the surface gratings ($l = 4$) almost completely eliminates coupling between them. As we show below, a much larger surface-mode transmission signal is achieved by the introduction of a central waveguide mode to mediate the coupling between the surface resonances.

For the L chip with $l = 4$ [Fig. 5(b)], the signature of the central waveguide mode appears as a pronounced transmission peak that redshifts in response to analyte-thickness increments. The peaks are much sharper than those for the S chip due to the higher quality factor of the central waveguide embedded in the PBG. The addition of surface modes to the L chip makes this waveguide mode more accessible to incident light. As shown below, the waveguide transmission peak broadens when the surface modes are added. In the absence of surface modes, the L chip behaves like a traditional high- Q resonance-shift biosensor. The only improvement here is that, within a PBG, it is possible to concentrate more light in the low-refractive-index region of the sensor without sacrificing resonance quality factor. This concentration simultaneously enables high sensitivity and a low limit of detection.

B. Biosensing with coupled resonances

We now incorporate both the surface and the line-defect modes into a single design to obtain what we refer to as the *LS chip* [Fig. 2(a)]. This chip provides our paradigm for multiparametric biosensing, in which analyte binding not only shifts individual resonance frequencies but also alters the coupling strengths between resonance modes. Consequently, different analyte combinations reveal distinct spectral fingerprints in the optical transmission. We note here that the chip thickness plays a crucial role in engineering the coupling between the modes, the details of which are in Appendix C.

We turn our attention to the transmission spectrum results for the LS chip in Fig. 6 for the case of no analyte binding ($t/a = 0$). The interaction of surface and

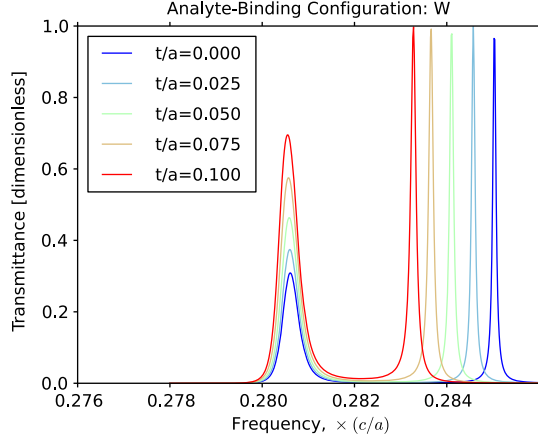


FIG. 6. FDTD results for the analyte binding at the W site for $l = 4$ of the LS chip. In addition to peak-shift biosensing by the WLM, the enhancement of the SLM transmission (due to enhanced indirect surface-mode coupling as a result of analyte binding) is a distinctive feature of our design.

line-defect modes clearly enhances the surface-mode transmission drastically when compared to Fig. 5(a) while broadening the line-defect resonance seen in Fig. 5(b), as expected. The transmission peak frequencies for the LS chip are slightly different from those of the S chip and the L chip due to stronger mode coupling. The coupled modes in the LS chip lead to linear combinations of the unhybridized surface and line-defect modes that we refer to as the *surfacelike modes* (SLMs) and *waveguidelike modes* (WLMs). While the SLMs have greater weight associated with the surface modes, the WLMs emphasize the line-defect modes. The resonance frequencies of the SLMs and WLMs are slight perturbations from the original surface and line-defect-mode frequencies, as delineated in Appendix B.

In what follows, we focus on the LS chip with $l = 4$, using FDTD spatial resolution of 80 mesh points per unit of periodicity. As noted in Appendix C, this value of $l = 4$ is the optimal chip thickness for establishing a weak coupling between surface and line-defect modes of the LS chip. For the $l \geq 4$ case, the coupling between the two unhybridized surface modes is sufficiently weak that there is a single SLM transmission peak (Fig. 6); i.e., the splitting in the two SLM frequencies calculated in Appendix B is small compared to the resonance linewidths. For $l < 4$, there are two distinguishable SLM peaks, as seen in Fig. 11(a) in Appendix C. From the discussion in Appendix C, we deduce that $l = 4$ provides the *optimal* coupling level between the optical modes of the device for biosensing.

We distinguish different analyte-binding configurations by the labels W, T, and B, referring to the central waveguide, top surface grating, and bottom surface grating, respectively. Analyte-binding configurations involving more than one site are likewise labeled WT, WB, BT, and WBT. Transmission spectra calculated with various thicknesses

of pure W binding are presented in Fig. 6. In the plots shown, we proceed in analyte-thickness increments that amount to two mesh steps in our FDTD calculations, i.e., $\delta t/a = 0.025 = 2/80$. As seen from Fig. 6, the spectral fingerprint of our device undergoes distinguishable changes as a result of these analyte-thickness increments. We demonstrate in Appendix C that our device is, in fact, capable of detecting analyte-thickness changes that are of the same order as the fabrication precision of the device. In Fig. 6, the peak due to the WLM progressively redshifts with increments to the analyte thickness, as in a conventional biosensor. On the other hand, for the SLM, the peak transmission level increases with the thickness of W binding. This change of transmission levels in one mode, due to analyte binding near another mode, is an important feature of our biosensor.

W binding redshifts the (unhybridized) line-defect mode, which is manifested as a redshift of the WLM. The redshift of the line-defect mode enhances the coupling between the unhybridized surface modes, which enhances the tunneling of photons from one surface mode to the other via the central waveguide. The net result is a transmission-level enhancement at the SLM resonance, in addition to a redshift of the WLM resonance.

As discussed in Appendix B, a coupling strength of μ (with units of frequency squared) between two degenerate modes with frequency ω results in the new frequencies $\sqrt{\omega^2 \pm |\mu|}$ for the hybridized modes. For the case of the degenerate surface modes (unhybridized) with frequency ω_S , it is shown in Appendix B that the SLMs attain frequencies of ω_S and $\sqrt{\omega_S^2 - [|\kappa|^2/(\omega_L^2 - \omega_S^2)]}$, where κ is the coupling strength (with units of frequency squared) between the surface and line-defect modes and ω_L is the unhybridized line-defect-mode frequency. The direct coupling between the top and bottom surface modes is negligible for the thick ($l = 4$) chip.

The indirect coupling between surface modes within the LS chip of $|\mu| = |\kappa|^2/(\omega_L^2 - \omega_S^2)$ is analogous to the quantum-mechanical expression of the *second-order perturbation theory* [23]. Photons in the bottom surface mode of frequency ω_S can tunnel to the intermediate off-resonant waveguide mode of frequency ω_L for a short time before tunneling again to the energy-conserving final state at the opposite surface. As the difference $(\omega_L^2 - \omega_S^2)$ becomes smaller, the indirect effective coupling is enhanced, even with very little change to κ . Analyte binding at W causes ω_L to redshift, bringing it closer to ω_S , and thereby enhancing the indirect interaction between the upper and lower surface modes. This enhancement manifests in greater SLM transmission. Therefore, in our multimode biosensor, analyte-induced frequency shifts also modify the effective coupling between modes, resulting in transmission enhancement or suppression behavior.

We now discuss the transmission spectral fingerprints for all the different possible analyte-binding configurations in

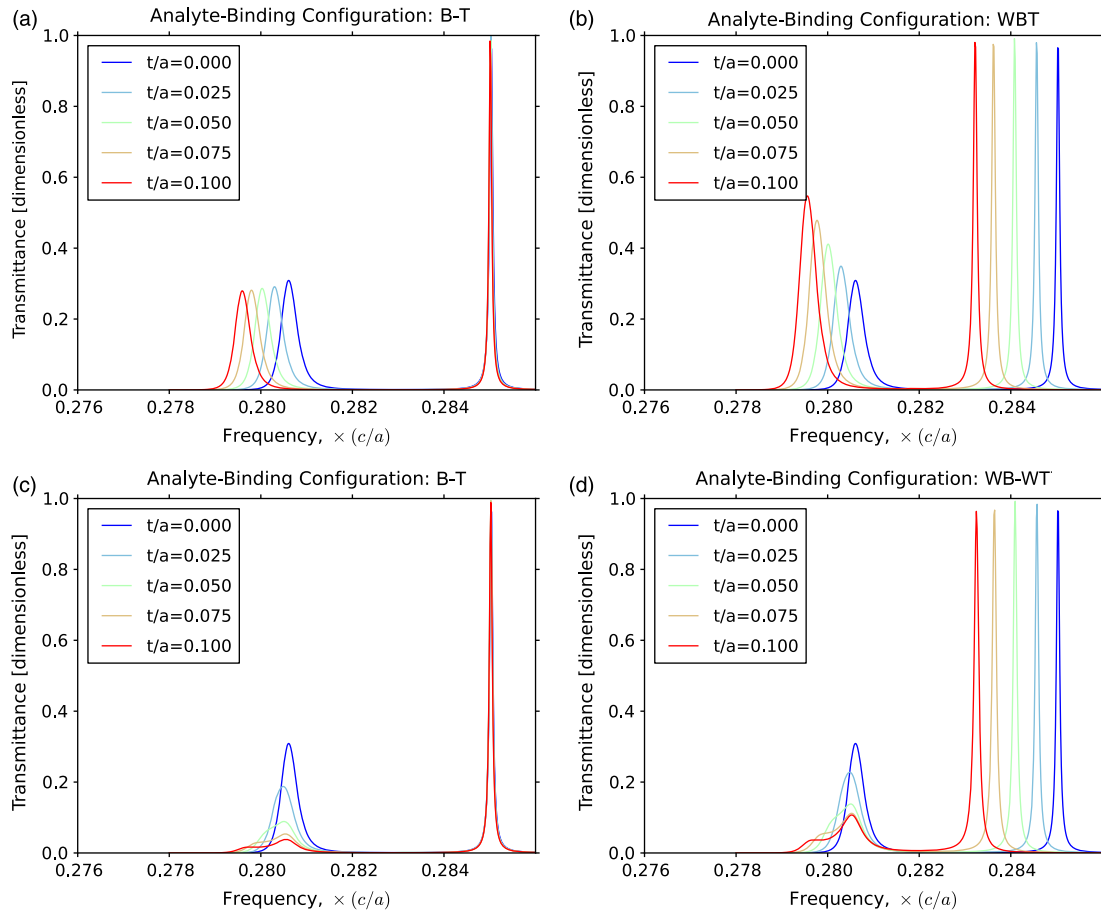


FIG. 7. Synopsis of results for four analyte-binding configurations in the LS chip. (a) BT: SLM redshift is observed with slight transmission suppression. (b) WBT: Both SLM and WLM redshifts occur, along with SLM transmission enhancement. (c) B-T: Lowering of SLM peak transmission and a splitting of the SLM peak occurs. (d) WB-WT: A WLM redshift occurs, along with SLM transmission suppression and peak splitting.

the LS chip. A synopsis of the four remaining analyte-binding scenarios that result in distinctive spectral fingerprints is presented in Fig. 7.

For BT analyte binding [Fig. 7(a)], the SLM transmission peak is redshifted as in a conventional surface-mode PC biosensor. The uniform analyte binding at B and T redshifts both of the unhybridized surface-mode frequencies equally. No appreciable change to the WLM peak is observed, indicating that the unhybridized line-defect mode is unaffected by surface binding. A slight reduction in the transmission levels is observed for the SLM resonance due to the increased frequency separation between the unhybridized surface and line-defect modes as a result of the redshift of the former.

For WBT analyte binding [Fig. 7(b)], we note that both the WLM and SLM transmission peaks are redshifted. The redshift increases with the uniform WBT analyte-layer thickness. In addition to this peak-shift behavior, the WBT binding configuration leads to enhancement of the SLM peak transmission level with a thickening of the analyte layers. This enhancement occurs because the

central-waveguide blocks (with larger surface area) receive more analyte than the surface-grating blocks. Therefore, the unhybridized line-defect mode is redshifted more than the surface modes. This variable redshift reduces $(\omega_L^2 - \omega_S^2)$, leading to enhanced indirect coupling between the surface modes, which allows more light to transmit through the LS chip in the SLM channel.

Because of the mirror symmetry of the chip about the central line-defect axis, analyte bindings at B and T are mutually indistinguishable in transmission, as are analyte bindings at WB and WT. Therefore, we discuss the results for B and T (WB and WT) as a single pair B-T (WB-WT). Both the B-T [Fig. 7(c)] and WB-WT [Fig. 7(d)] configurations exhibit a suppression in the SLM peak transmission levels. In addition to the transmission suppression, the SLM channel is seen to split into two distinct peaks beyond a certain threshold of analyte thickness. The separation of the two SLM peaks becomes perceptible for $t/a \gtrsim 0.050$ [Figs. 7(c) and 7(d)]. Analyte binding at one of the two available surfaces redshifts the corresponding unhybridized surface mode. For the $l = 4$ case, the SLM frequencies are

almost degenerate (cf. Appendixes B and C for more details). For a significant redshift of one of the surface modes, the SLM transmission peak splits into two peaks, suppressing SLM transmission. The corresponding shift away from the line-defect-mode frequency results in fewer photons being able to tunnel through the chip by hopping from the entry surface, through the central line defect, to the exit surface. This result is manifest in the overall transmission suppression. Despite the similar behavior of the SLM transmission peaks, the WB-WT bindings are distinct from the B-T bindings. The former involve redshifts to the WLM resonance peak. Consequently, the frequency-overlap reduction between the unhybridized surface modes and the waveguide mode is less pronounced compared to the B-T binding. As a result, the SLM transmission suppression is less drastic for the WB-WT binding.

Key features of the transmission spectral fingerprints of Figs. 6 and 7 are shown in Fig. 8. We track the WLM resonance frequencies, as well as SLM resonance frequencies and transmission levels, when two peaks are present in the spectrum. A *least-squares fitting method*, based on three Lorentzian functions, is employed to facilitate tracking of the split SLM peaks and their suppressed transmission levels at $t/a \geq 0.050$ for B-T and WB-WT analyte bindings.

We note that the behavior of the WLM in our biosensor is very much akin to that of a traditional resonance-shift biosensor for all analyte-binding configurations involving the W site—i.e., for W, WB-WT, and WBT. It is only for these configurations that there is a redshift of the WLM peak [Fig. 8(a)]. We note here that the slopes of plots in Fig. 8(a) give the resonance-shift sensitivity values of the WLM. The peak WLM transmission remains at almost 100% for all analyte-binding configurations. Traditional resonance-shift biosensing is also demonstrated for the SLM in Fig. 8(b), where the slopes of the plots represent the resonance-shift sensitivity of the LOC device. Plots in Fig. 8(c) track the SLM peak transmission levels as enhanced or suppressed by analyte binding, and their slopes quantify the peak transmission-level sensitivity for the analyte-binding configurations shown.

A summary of the detection capability of multiple disease markers by our biosensor is presented in Table I. There are six distinctive signatures in the transmission signal for the various analyte-binding configurations. In order to elucidate the six different cases detectable, we consider three different biological markers labeled α , β , and γ , which attach to the sites T, B, and W, respectively. Our biosensor distinguishes the following cases:

$$\left\{ \begin{array}{l} (\text{NOT } \alpha) \text{ AND } (\text{NOT } \beta) \\ \alpha \text{ XOR } \beta \\ \alpha \text{ AND } \beta \end{array} \right\} \otimes \left\{ \begin{array}{l} \text{NOT } \gamma \\ \gamma \end{array} \right\}.$$

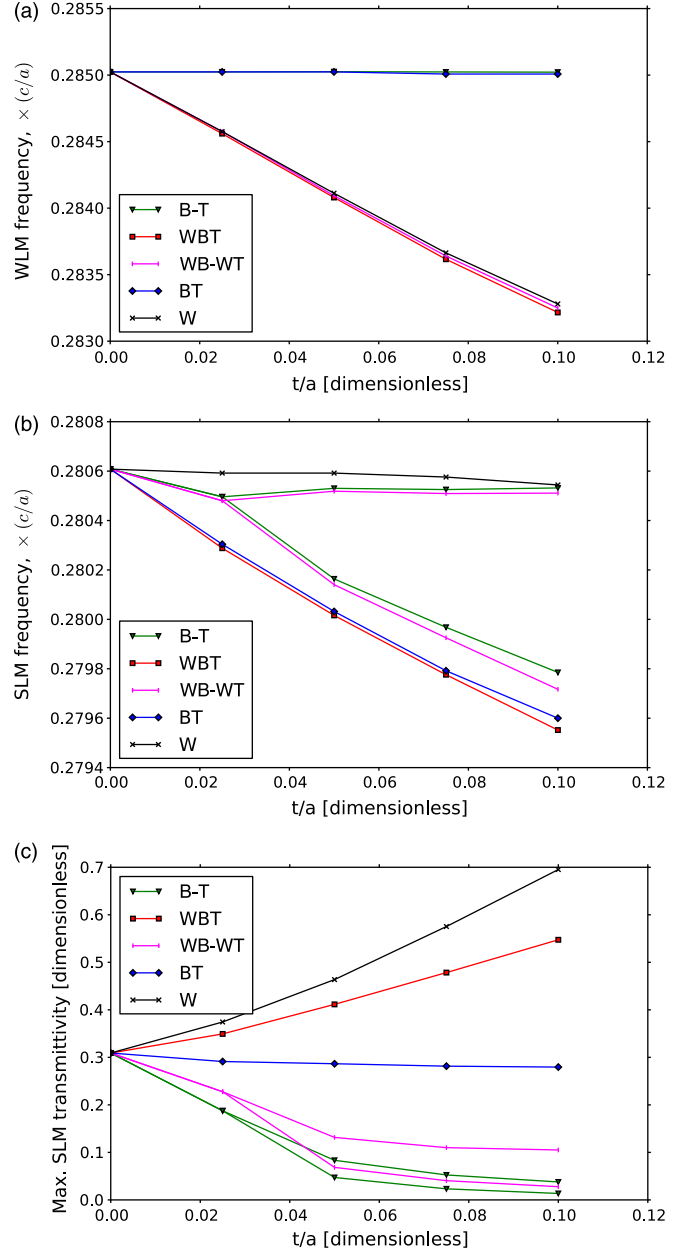


FIG. 8. Spectral fingerprints of the transmission spectrum data for the $l = 4$ LS chip in response to analyte binding. (a) WLM peak positions: Analyte binding at W is required for a response. (b) SLM peak positions: Splitting of peaks is seen for asymmetric top and bottom surface analyte binding. (c) SLM peak transmission levels: Increased frequency overlap between surface and line-defect modes enhances peak transmission. Slopes define *peak transmission-level sensitivity*.

C. Referencing the biosensor against spurious environmental factors

For this section, we discuss both the $l = 3$ and the $l = 4$ LS chips. An important feature of our LS-chip biosensor for $l = 3$ is that one of the SLM peaks does not shift due to W binding as seen in Fig. 9. We note that the FDTD results in Fig. 9 are based on a spatial resolution of 40 mesh points

TABLE I. Transmission spectrum response to the increase of analyte-layer thickness for the various analyte-binding configurations. The frequency shifts of the WLM and the frequency shifts, transmission levels, and peak-splitting characteristics of the two SLMs provide the means for differentiating between various analyte-binding configurations.

Analyte-binding configuration	ω_{WLM}	ω_{SLM}	T_{SLM}	ω_{SLM} split?
(NOT α) AND (NOT β) AND (NOT γ)			—	N
(NOT α) AND (NOT β) AND γ	←		↑	N
(α XOR β) AND γ	←		↓	Y
(α XOR β) AND (NOT γ)			↓	Y
α AND β AND γ	←	←	↑	N
(α AND β) AND (NOT γ)		←	↓	N

per unit of periodicity. Electric field snapshots for the SLMs and WLM in Fig. 9 are shown in Fig. 10. As discussed in Appendix B, the SLM in Fig. 9 that is insensitive to W binding is an antisymmetric linear combination of the top and bottom surface modes. The waveguide line defect is centered at a nodal line of this mode, as seen from Fig. 10(b). Consequently, this mode is insensitive to refractive-index changes near the waveguide. On the other hand, the other SLM—approximated by a symmetric linear combination of the upper and lower surface modes—exhibits a notable response to W binding, having a notable presence of fields near this binding site [Fig. 10(a)].

Spurious signal changes due to environmental factors, such as temperature fluctuations, are common problems in a biosensor [24]. Temperature fluctuations change the analyte refractive index, disrupting the calibration of the device for measuring the analyte thickness. A *referencing mechanism* that provides a baseline to be established for measurements is valuable in this context. The

antisymmetric SLM is useful for such referencing. As shown in Appendix B, the antisymmetric SLM has a frequency equal to that of the unhybridized surface mode. While insensitive to W binding, it is sensitive to the refractive index of the fluid medium. This discrimination provides a tool to monitor changes in ambient conditions, like temperature, that alter refractive-index values for the fluid and analyte.

For example, we consider an artificially enhanced analyte refractive index ($n_{\text{an}} > 1.45$) due to temperature fluctuations, etc. A thinner layer of this higher-index analyte may cause a frequency shift equal to that of a thicker layer of regular-index analyte. In the absence of a referencing mechanism for the analyte refractive index, the sensor will be incorrectly calibrated, leading to an artificially amplified frequency shift and a subsequent overrepresentation of the analyte thickness. A more detailed discussion for n_{an} variation is presented in Appendix D. The position of the antisymmetric SLM peak can be used to probe the ambient conditions due to its sensitivity to conditions of the fluid environment, thus establishing a benchmark for the analyte-thickness sensitivity based on the correct refractive index. For this calibration of the analyte refractive index to be useful, a compendium of the behavior of the sensor over a range of analyte and fluid-medium refractive indices has to be established. Typical results are shown in Appendix D.

For referencing, the $l = 3$ LS chip can be used to supplement detections in the $l = 4$ chip. Both the detector and the reference chips can receive the same sample by means of a “split-mesa” superchip that fabricates the two chips side by side [25]. The biorecognition occurs in the $l = 4$ chip. Two spectral measurements are taken from the superchip: one for the reference and one for the detection.

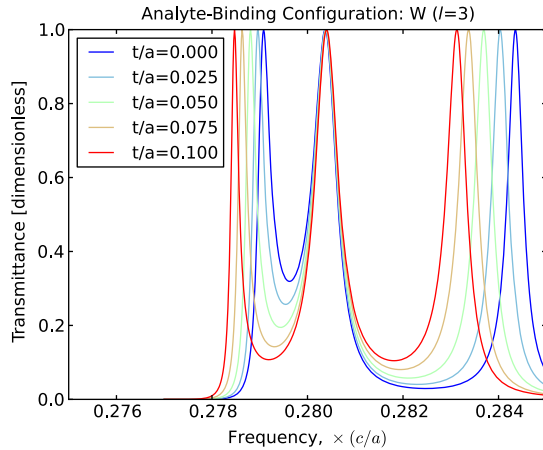


FIG. 9. Insensitivity of the antisymmetric SLM to analyte binding at W. There are three distinct peaks due to two SLMs and one WLM. The unhybridized surface modes interact directly. The antisymmetric SLM peak is insensitive to analyte binding at W. This SLM peak can be used to establish a benchmark for the fluid refractive index for referencing against environmental factors.

D. Practical considerations

We have discounted considerations of light coupling into the glass superstrate-substrate regions from an air environment as may be expected to be the case for an experimental setup. This issue of light coupling needs to be addressed in detail for an operational sensor based on our prototype.

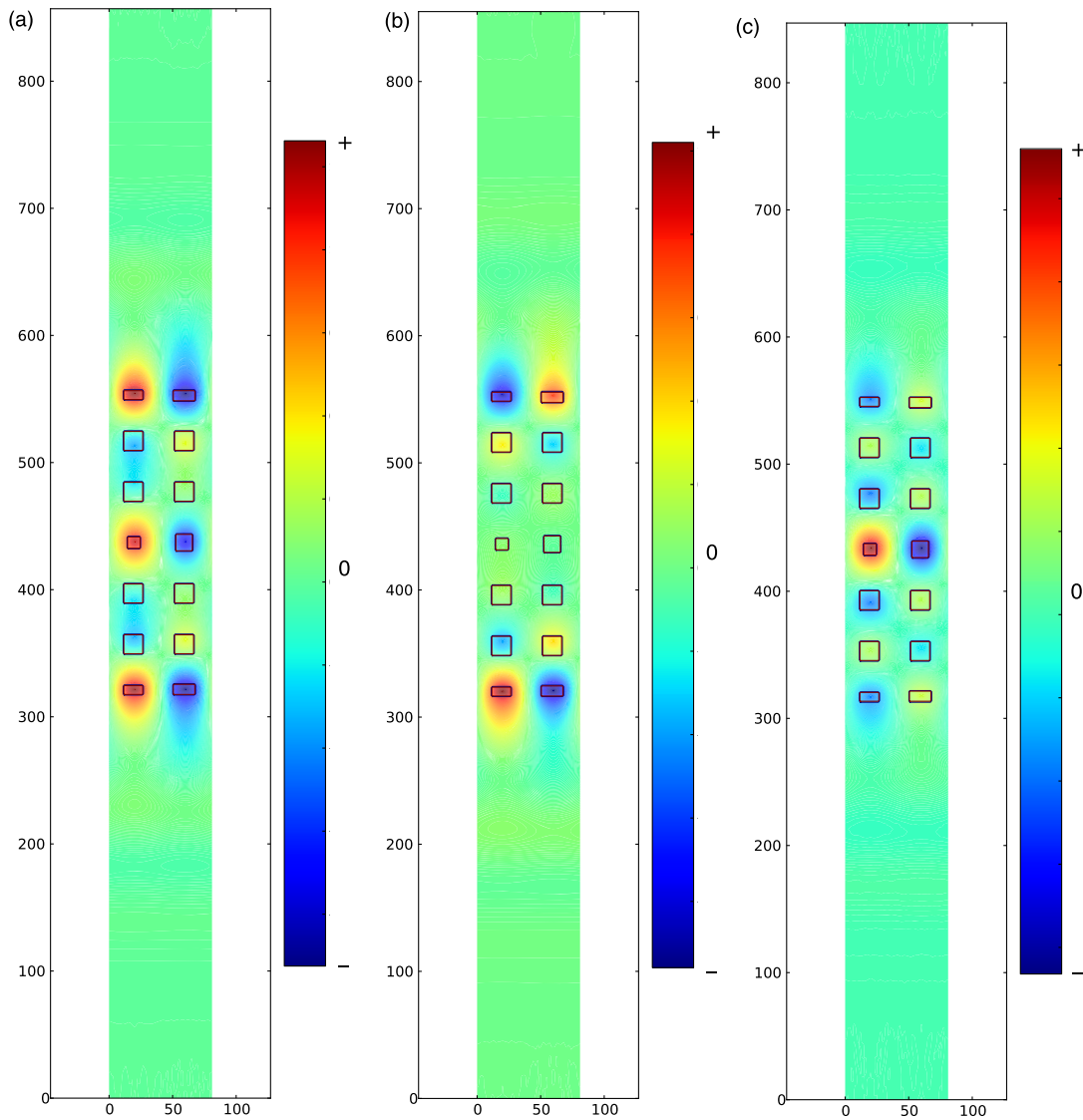


FIG. 10. Electric field snapshots (arbitrary units) illustrating the mode characteristics for $l = 3$ at a resolution of 40 mesh steps per unit of periodicity. (a) Symmetric linear combination of surface modes at $(\omega a)/(2\pi c) = 0.2791$: The waveguide region is illuminated by an antinode of the field. (b) Antisymmetric linear combination of surface modes at $(\omega a)/(2\pi c) = 0.2803$: The waveguide region is at a node of the field. (c) Waveguidelike mode at $(\omega a)/(2\pi c) = 0.2843$: The field energy is mostly concentrated at or near the central line defect.

The results presented here are, primarily, conceptual in nature. However, our conceptual prototype may be conveniently extended to involve the guided modes of a more readily fabricated, and structurally stable, PC shown in Fig. 2(c). This 3D woodpile architecture consists of alternating layers of planar gratings lying orthogonally to each other. Our 2D geometry is structurally similar to a section through the 3D simple-cubic woodpile depicted [Fig. 2(c)]. Our squares correspond to logs of the simple-cubic woodpile oriented only along a certain direction. In order to achieve a complete 3D PBG, it is necessary to replace the simple-cubic woodpile with a face-centered cubic (diamond-structure) woodpile [26]. The fabrication

of such 3D woodpiles, along with engineering of defects thereof, is well documented [27,28].

V. CONCLUSION

We present the conceptual prototype of a LOC optical biosensor based on a finite-sized PBG material embedded in a glass slide and interspersed with microfluidic channels. A sensing mechanism based on weak coupling of the PBG surface and line-defect waveguide modes is numerically demonstrated. FDTD calculations are used to establish that a conventional resonance peak-shift approach can be supplemented by transmission suppression or enhancement

effects in order to facilitate the detection of variable amounts of thin-layer analytes. Unlike previous biosensors that rely exclusively on analyte-induced changes to a single optical resonance mode, our detection scheme includes the effects of analyte-induced changes to the coupling between nearby optical resonances in frequency space. This scheme leads to more detailed spectral fingerprints of samples containing a mixture of various disease markers. The mode volumes of our optical resonances cover a large volume fraction of the entire LOC. In the mousetrap analogy, this coverage enables the mice (disease markers) to readily find their traps (binding sites), which reduces the required sample volume and time required for detection to occur. Most significantly, we demonstrate that our sensing strategies enable the quantitative detection of six different combinations of up to three separate biological markers. This result offers a valuable mechanism for the diagnosis of diseases characterized by the presence of multiple biological factors in a diagnostic sample.

ACKNOWLEDGMENTS

We are grateful to J. H. Jiang, W. T. Lau, A. Gandhi, and S. Eyderman for helpful discussions. Financial support was provided by the Natural Sciences and Engineering Research Council of Canada and the United States Department of Energy under Contract No. DE-FG02-06ER46347.

APPENDIX A: OPERATIONAL DEFINITIONS OF SENSITIVITY AND LIMIT OF DETECTION FOR RESONANCE-SHIFT BIOSENSING

The *resonance-shift sensitivity* for the m th mode of our biosensor is defined as the rate of change of resonance frequency, ω_m , with analyte-layer thickness t :

$$S_m \equiv \frac{\partial \omega_m}{\partial t}. \quad (\text{A1})$$

An estimate [29] of this sensitivity is found by using the *first-order perturbation theory* on the Maxwell wave equation. The shift $\delta\omega_m$ in resonance frequency for “small” increments δt to the analyte-layer thickness is approximated [by using the electric field pattern $\mathbf{E}_m(\mathbf{r})$ and the dielectric constants of the analyte, ϵ_A , and the fluid, ϵ_F] as a ratio of two integrals—one over the “area” of the fluid-analyte interface regions, I , and the other over the entire supercell volume S of the PC:

$$\delta\omega_m = \omega_m \mathfrak{F}_m \delta t + O((\delta t)^2). \quad (\text{A2})$$

The *optical field concentration of the m th mode at the analyte-binding interface*, \mathfrak{F}_m , is given by [29]

$$\mathfrak{F}_m \equiv -\frac{1}{2} \frac{\int_I [(\epsilon_A - \epsilon_F) |\mathbf{E}_{m,\parallel}(\mathbf{r})|^2 - (\epsilon_A^{-1} - \epsilon_F^{-1}) |\epsilon(\mathbf{r}) \mathbf{E}_{m,\perp}(\mathbf{r})|^2] d^{D-1}\mathbf{r}}{\int_S \epsilon(\mathbf{r}) |\mathbf{E}_m(\mathbf{r})|^2 d^D\mathbf{r}}. \quad (\text{A3})$$

Here, $\mathbf{E}_{m,\parallel}(\mathbf{r})$ is the component of the electric field directed tangentially along the interface I , while $\mathbf{E}_{m,\perp}(\mathbf{r})$ is the component normal to the interface. For a D -dimensional system, integration in the numerator is in $(D-1)$ dimensions, whereas the integral in the denominator is in D dimensions ($D=2$ for our system). Clearly, the *resonance-shift sensitivity* is as shown in Eq. (2):

$$S_m \equiv \frac{\delta\omega_m}{\delta t} = \omega_m \mathfrak{F}_m.$$

The sensitivity is proportional to the optical field concentration at the fluid-analyte interface. The higher the proportion of the mode energy that is concentrated at the interface I , the larger the frequency shift in response to the analyte binding. For our 2D LOC with only the TM polarization, there are no electric field components perpendicular to the analyte-fluid boundary regions. In other words, $\mathbf{E}_m(\mathbf{r}) = E_m^{(z)}(\mathbf{r}) \hat{\mathbf{z}} = \mathbf{E}_{m,\parallel}(\mathbf{r})$ and $\mathbf{E}_{m,\perp}(\mathbf{r}) = \mathbf{0}$.

The *resonance-shift limit of detection* $t_m^{(\text{lim})}$ is obtained from the resolvability of two closely located spectral resonance peaks with and without analyte binding, with frequencies ω'_m and ω_m , respectively. We assume that a frequency separation of $\eta\Delta\omega_m$ is required to claim a “detection,” where η is a number, of the order of unity, defined by the specific detection system. $\Delta\omega_m$ is the full width at half maximum (FWHM) of the spectral line located at ω_m ($\Delta\omega_m \approx \Delta\omega'_m$ may be assumed for small changes to t). The analyte-layer thickness required for optical detection is defined as

$$t_m^{(\text{lim})} \equiv \frac{\eta\Delta\omega_m}{S_m}. \quad (\text{A4})$$

Using the relationship between the sensitivity and the optical field concentration, \mathfrak{F}_m , as well as the definition of the quality factor, $Q_m = \omega_m/\Delta\omega_m$, we arrive at Eq. (3):

$$t_m^{(\text{lim})} \equiv \frac{\eta\Delta\omega_m}{S_m} = \frac{\eta}{\mathfrak{F}_m Q_m}.$$

APPENDIX B: SIMPLIFIED MODE-COUPLING MODEL OF THE PHOTONIC-BAND-GAP RESONANCES

We consider an operator form of the Maxwell wave equation (1) written as (setting $c = 1$ for convenience)

$$\Theta|\mathbf{H}_{j,\mathbf{k}}\rangle = [\omega_j(\mathbf{k})]^2|\mathbf{H}_{j,\mathbf{k}}\rangle. \quad (\text{B1})$$

1. Degeneracy lifting of surface modes in the $l = 3$ S chip

We consider a PC chip with two degenerate surface modes $|s_1\rangle$ and $|s_2\rangle$ at the Γ point ($\mathbf{k} = \mathbf{0}$)—corresponding to the top and the bottom surface modes of the chip—with an eigenfrequency ω_S . In a small neighborhood of frequency space centered around $\omega = \omega_S$, the operator in the PC wave equation can be approximated for the case of noninteracting degenerate surface modes as

$$\Theta \approx \Theta_0 = \omega_S^2(|s_1\rangle\langle s_1| + |s_2\rangle\langle s_2|). \quad (\text{B2})$$

Here, we use the fact that the PBG has removed all other modes in this frequency range within the chip. By introducing a weak coupling κ (with dimensions of frequency squared), between $|s_1\rangle$ and $|s_2\rangle$, the Maxwell operator becomes

$$\Theta \approx \Theta_1 = \Theta_0 + \kappa|s_1\rangle\langle s_2| + \kappa^*|s_2\rangle\langle s_1|. \quad (\text{B3})$$

The foregoing is a 2×2 matrix in the $\{|s_1\rangle, |s_2\rangle\}$ basis:

$$M_1 = \begin{bmatrix} \omega_S^2 & \kappa \\ \kappa^* & \omega_S^2 \end{bmatrix}. \quad (\text{B4})$$

This matrix has eigenvalues:

$$\xi_{\pm} = \omega_S^2 \pm |\kappa|. \quad (\text{B5})$$

These eigenvalues are associated with the *antisymmetric* and *symmetric* linear combinations of the original surface modes.

2. Hybridization of surface and line-defect modes in the $l = 4$ LS chip

For a thicker $l = 4$ chip, we assume no direct coupling between the surface modes $|s_1\rangle$ and $|s_2\rangle$. They remain degenerate with frequency ω_S . A central line-defect mode $|l\rangle$ is introduced with frequency ω_L . We choose $\omega_L > \omega_S$. In the absence of coupling between the modes, the Maxwell operator in Eq. (B1) is

$$\Theta \approx \Theta_0 = \omega_S^2(|s_1\rangle\langle s_1| + |s_2\rangle\langle s_2|) + \omega_L^2|l\rangle\langle l|. \quad (\text{B6})$$

As before, we assume that the PBG excludes all other modes with nearby frequencies in the chip. We now

introduce a weak evanescent coupling between the surface and line-defect modes but assume negligible coupling between the two surface modes. The Maxwell operator becomes

$$\Theta \approx \Theta_1 = \Theta_0 + \kappa_1|s_1\rangle\langle l| + \kappa_1^*|l\rangle\langle s_1| + \kappa_2|s_2\rangle\langle l| + \kappa_2^*|l\rangle\langle s_2|. \quad (\text{B7})$$

By symmetry, the coupling strength between the upper surface mode and the central line-defect mode is the same as the coupling strength between the lower surface mode and the central line-defect mode. In other words, $\kappa_1 = \kappa = \kappa_2$. In the $\{|s_1\rangle, |s_2\rangle, |l\rangle\}$ basis, the operator is a 3×3 matrix:

$$M_1 = \begin{bmatrix} \omega_S^2 & 0 & \kappa \\ 0 & \omega_S^2 & \kappa \\ \kappa^* & \kappa^* & \omega_L^2 \end{bmatrix}. \quad (\text{B8})$$

Its eigenvalues ξ satisfy the cubic equation (B9):

$$(\xi - \omega_S^2)[\xi^2 - (\omega_L^2 + \omega_S^2)\xi + (\omega_S^2\omega_L^2 - 2|\kappa|^2)] = 0. \quad (\text{B9})$$

The solutions to Eq. (B9) are $\xi = \omega_S^2$ and

$$\xi = \frac{1}{2}[(\omega_L^2 + \omega_S^2) \pm \sqrt{(\omega_L^2 - \omega_S^2)^2 + 8|\kappa|^2}]. \quad (\text{B10})$$

In the *weak coupling limit* defined by the condition $|\kappa| \ll (\omega_L^2 - \omega_S^2)$, using the fact that $\omega_L > \omega_S$, the eigenvalues become

$$\xi = \omega_S^2, \quad \xi \approx \omega_S^2 - \frac{2|\kappa|^2}{\omega_L^2 - \omega_S^2}, \quad \omega_L^2 + \frac{2|\kappa|^2}{\omega_L^2 - \omega_S^2}. \quad (\text{B11})$$

These correspond to three resonance peaks in the optical transmission through the LS chip, as seen for $l = 3$ in Fig. 9, whereas the $|\kappa| \rightarrow 0$ limit is reached for $l > 3$ in Figs. 11(a) and 11(b) (cf. Appendix C). As a result of the off-diagonal interaction terms in our matrix, perturbed frequencies (squared) have corrections analogous to *second-order perturbations* in quantum-mechanical systems [23].

a. Antisymmetric surfacelike mode at $\xi = \omega_S^2$

The eigenvector of M_1 corresponding to the eigenvalue $\xi = \omega_S^2$ is an *antisymmetric linear combination of the surface modes* given by $[+2^{-1/2}, -2^{-1/2}, 0]^T$ (whether or not the limit $|\kappa| \rightarrow 0$ applies). There is no influence of the line-defect modes at all for this SLM.

b. Symmetric surfacelike mode at $\xi \approx \omega_S^2 - \frac{2|\kappa|^2}{\omega_L^2 - \omega_S^2}$

In the limit $|\kappa| \rightarrow 0$, the mode frequency $\xi \approx \omega_S^2 - \frac{2|\kappa|^2}{\omega_L^2 - \omega_S^2}$ becomes degenerate with the antisymmetric SLM, but with eigenvector $[+2^{-1/2}, +2^{-1/2}, 0]^T$. Therefore, this SLM is a *symmetric linear combination of the surface modes*. For the case of non-negligible κ , this SLM corresponds to the lowest frequency in the transmission spectrum (as seen for the $l=3$ case of the LS chip in Fig. 9). This SLM involves slight mixing of the central line-defect mode.

c. Waveguidelike mode at $\xi \approx \omega_L^2 + \frac{2|\kappa|^2}{\omega_L^2 - \omega_S^2}$

For the case of $\xi \approx \omega_L^2 + \frac{2|\kappa|^2}{\omega_L^2 - \omega_S^2}$, in the limit $|\kappa| \rightarrow 0$, $\xi \approx \omega_L^2$, with an eigenvector $[0, 0, 1]^T$. As a result, the eigenstate is essentially a line-defect mode. When the limit $|\kappa| \rightarrow 0$ is not strictly satisfied, this eigenstate may be called a WLM with some weak mixing with the surface modes.

d. Mode structure for $\omega_L \approx \omega_S$

In the situation where $\omega_L \approx \omega_S$, the exact solution of the cubic eigenvalue equation (B9) must be considered. While the antisymmetric SLM at $\xi = \omega_S^2$ is retained with its previous interpretation, the other eigenvalues become $\xi \approx \frac{1}{2}(\omega_S^2 + \omega_L^2) \pm |\kappa|\sqrt{2}$. These eigenvalues are both based on a symmetric combination of surface modes, with the central waveguide and surface-mode amplitudes having either the same sign or the opposite sign. The central waveguide field intensity is roughly twice that of either surface region. This result leads to a distinctive three-peak signature in the transmission structure as discussed in Appendix D.

APPENDIX C: THE EFFECTS OF CHIP THICKNESS AND FABRICATION PRECISION

1. Optimal chip thickness

Here, we address the question of optimum thickness of our LOC biosensor. If the chip thickness is too small ($l \leq 3$), the Q factor of the transmission resonances becomes small, and the resonance-shift limit of detection becomes poor. On the other hand, when the chip is too thick ($l \geq 5$), the transmission resonances become very narrow and are easily dominated by disorder from fabrication imperfections.

We concentrate here on the LS chip shown in Fig. 2(a), with $l \in \{3, 4, 5\}$. All the FDTD calculations here are undertaken with a spatial resolution of 40 mesh points per unit of lattice periodicity a . The FDTD spatial resolution is representative of the fabrication precision; i.e., the device may have imperfections of up to the order of the FDTD

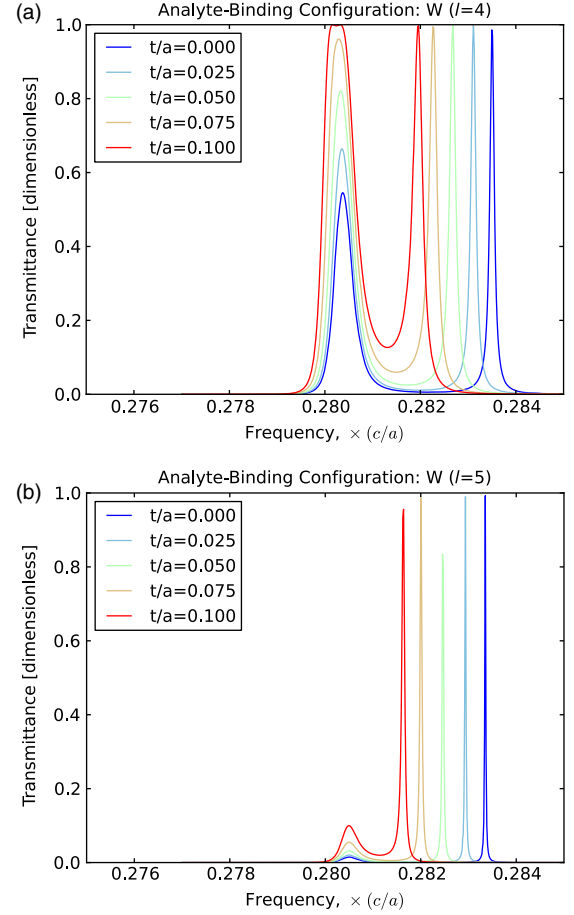


FIG. 11. Effects of LS-chip thickness on the transmission for analyte binding at W. (a) $l=4$: There are now only two distinct peaks due to merging of the previously distinct SLM peaks. The unhybridized surface modes have little direct interaction. (b) $l=5$: The SLM peaks are very faint, and the extremely weak mode couplings are less suitable for multiparametric biosensing. (Note: Cf. Fig. 9 for the case of $l=3$.)

mesh-step size. For illustration, we consider only W binding.

Calculated transmission spectra for the three chip thicknesses are presented in Figs. 9 and 11. For the $l=3$ chip in Fig. 9, the original surface and waveguide modes, in the absence of analyte binding, are well coupled due to their spatial proximity. The presence of a non-negligible coupling between the two surface modes is manifest in the dual-peak signature of the SLMs in the transmission spectrum (cf. Appendix B for details). Moreover, there is a pronounced frequency separation between the transmission peaks for the SLMs and the WLM. SLM transmission enhancement with analyte binding—observed for the $l=4$ and $l=5$ LS chips—is not observed.

As discussed in Appendix B, the SLMs can be considered as symmetric and antisymmetric linear combinations of the unhybridized surface modes. On the other hand, the

WLM consists mostly of optical fields concentrated near the waveguide line-defect region of the LS chip. Electric field snapshots for the $l = 3$ chip, presented in Fig. 10, lend support to the mode characteristics expected from a linear combination of surface and line-defect modes. As discussed in Appendix B, the lower-frequency SLM is roughly a *symmetric* linear combination of the surface modes. The field map in Fig. 10(a) at frequency $(\omega a)/(2\pi c) = 0.2791$ confirms this interpretation, revealing a distinct nonzero optical field concentration equidistant from the two surfaces (near the line-defect region) as well as a symmetric field distribution above and below the line defect. The fields in Fig. 10(b) almost vanish near the central line defect, and amplitudes are antisymmetric about the central line defect, confirming that the higher-frequency $[(\omega a)/(2\pi c) = 0.2803]$ SLM is an *antisymmetric* linear combination of the surface modes. Figure 10(c) reveals that the mode at $(\omega a)/(2\pi c) = 0.2843$ is a WLM.

The symmetric SLM for $l = 3$ is sensitive to analyte binding at the W site, whereas the antisymmetric SLM is not [Figs. 9, 10(a), and 10(b)]. In the case of $l > 3$, the symmetric and antisymmetric SLM transmission peaks are no longer distinguishable. The overall transmission enhancement of the SLMs for $l > 3$ from W binding is due to the waveguide-mediated surface-mode coupling, as explained earlier.

As seen from Figs. 10(a) and 10(b), the symmetric SLM has lower frequency than the antisymmetric one and is sensitive to W binding. For an analyte having a higher refractive index than the background fluid, the symmetric SLM undergoes a redshift (by the *first-order perturbation theory* [29]). This redshift moves the symmetric SLM transmission peak even lower in frequency relative to the antisymmetric SLM. This response to W binding is evident in the spectra for the $l = 3$ chip (Fig. 9).

The $l = 3$ chip exhibits direct surface-surface coupling. This coupling is indicated by the fact that, for each of the SLM and WLM peaks, the peak transmission remains almost 100%. A larger value for l is desirable to operate in the highly responsive weak-coupling regime between guided modes. In this regime, the SLM frequencies are nearly degenerate.

Inspection of Figs. 11(a) and 11(b) reveals that the $l = 4$ chip provides the optimal chip thickness for multiparametric biosensing. It exhibits a single SLM peak for W binding that can split into two peaks with B-T binding as well as WB-WT binding. There is also a reasonable free spectral range between the SLM and WLM peaks, allowing for frequency-shift biosensing using the WLM. Moreover, the frequency separation of the WLM and the SLMs is ideal for transmission changes to occur significantly with analyte-thickness changes (Fig. 12). For the $l = 5$ chip, the coupling between modes becomes too weak, the overall transmission intensities drop significantly, and the spectral

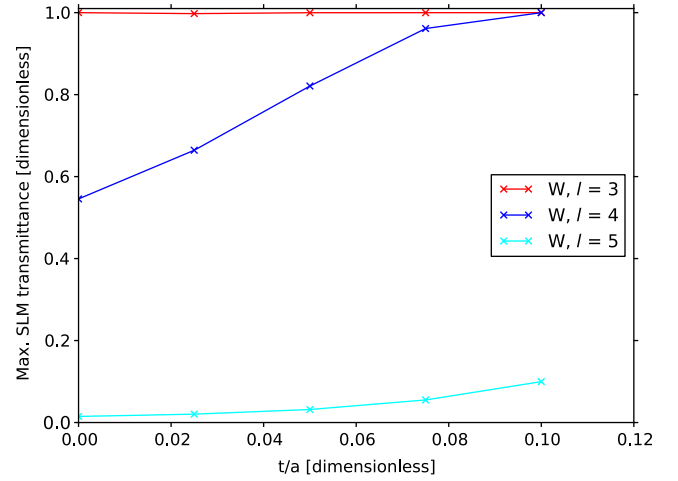


FIG. 12. Peak transmission vs analyte thickness in W binding for various LS-chip thicknesses. The most conspicuous changes to the transmission levels are observed for the $l = 4$ case, which constitutes the best choice for the coupling level between the surface and line-defect modes of the biosensor device. In other words, the choice of optimal chip thickness is dictated largely by optimal peak transmission-level sensitivity.

response of the biosensor deteriorates considerably with fabrication-induced disorder.

2. Comparison of W binding in the $l = 4$ LS chip for different fabrication precisions

We now compare the performance of the $l = 4$ LS chip for resolutions of 40 and 80 mesh steps per lattice period. This comparison is an indicator of its performance for different degrees of precision in fabrication. From comparisons of spectral data, it is found that the resonance-shift sensitivities of the WLM and the SLMs for the W-binding configuration are comparable for both resolutions, with the higher-resolution results being marginally better. We conclude that the resolution does not have a very significant effect on the resonance-shift sensitivity. However, Q factors are lower for modes calculated with lower resolution. For example, in the WLM with no analyte binding ($t/a = 0$), $Q \approx 3500$ at a resolution of 80 mesh steps per unit of periodicity, while for the same value of the analyte thickness, $Q \lesssim 3000$ at a resolution of 40 mesh steps per unit of periodicity. It is well known that a lower precision of fabrication compromises the Q factors of resonant modes.

Comparing the high- and low-resolution results for the W-binding case of $l = 4$ [Figs. 6 and 11(a), respectively], it is seen that the position of the low- Q SLM peak for $t/a = 0$ is essentially oblivious to resolution, but the high- Q WLM peak occurs at a lower frequency for the lower-precision FDTD results. The coarser subpixel averaging of the low-resolution case leads to a larger overall index for the waveguide region, leading to a lower frequency for the WLM. Such resolution-dependent changes to the position of high- Q resonances are a known FDTD issue.

Nonetheless, the interaction of the WLM and SLM leading to SLM peak transmission enhancements is observed for both resolutions. Therefore, it is still possible to obtain a detailed spectral fingerprint under different fabrication precisions for the device.

We also note that our proposed biosensor is *capable of detecting analyte-thickness changes that are of the same order as the fabrication accuracy* of the PC chip. For a spatial resolution of 40 mesh points per lattice period, a (mesh size of $\Delta = a/40$), our system distinguishes changes to analyte-layer thickness of $\delta t = \Delta$, i.e., $\delta t/a = 0.025$. Our device nevertheless still needs to conform to a high degree of fabrication fineness. For example, if $\delta w_{\text{sg}}/a = 0.05$ instead of $\delta w_{\text{sg}}/a = 0.10$ and $\delta w_{\text{wg}}/a = 0.05$ instead of $\delta w_{\text{wg}}/a = 0.10$, the transmission for the frequency window considered is uniformly zero.

APPENDIX D: VARIATION OF ANALYTE REFRACTIVE INDEX

Here, we present some details due to the variation of the analyte refractive index n_{an} . The FDTD results discussed are based on a spatial resolution of 40 mesh points per unit of periodicity, with $1.35 \leq n_{\text{an}} \leq 1.55$ and $t/a = 0.01$.

Figure 13 depicts transmission spectra for the BT, W, and WB-WT analyte-binding cases. In Fig. 13(a), for the BT-binding case, the SLMs are seen to redshift with progressive enhancement of n_{an} . The W and WB-WT cases depicted in Figs. 13(b) and 13(c), respectively, present some intricacies, particularly for the case of $n_{\text{an}} = 1.50$. For the spectral signature for the W case in Fig. 13(b), instead of the usual two-peak signature seen for other n_{an} values, there is an anomalous three-peak signature at $n_{\text{an}} = 1.50$. Analyte binding redshifts the intrinsic line-defect-mode frequency ω_{L} , bringing it very close to the intrinsic surface-mode frequency ω_{S} , causing $\omega_{\text{L}} \approx \omega_{\text{S}}$. As discussed in Appendix B, while the central peak is still due to the antisymmetric SLM, the two peripheral peaks are due to two strongly hybridized modes and involve the symmetric combination of the surface modes which are in phase or out of phase with the line-defect mode. In the case of the WB-WT binding in Fig. 13(c), the three-peak transmission scenario for the larger values of n_{an} is due to SLM peak splitting, observed earlier, as well as due to the $\omega_{\text{L}} \approx \omega_{\text{S}}$ situation around $n_{\text{an}} = 1.50$. Similar effects of $\omega_{\text{L}} \approx \omega_{\text{S}}$ will occur for certain combinations of n_{an} and t and must be accounted for during the calibration and operation of the sensor.

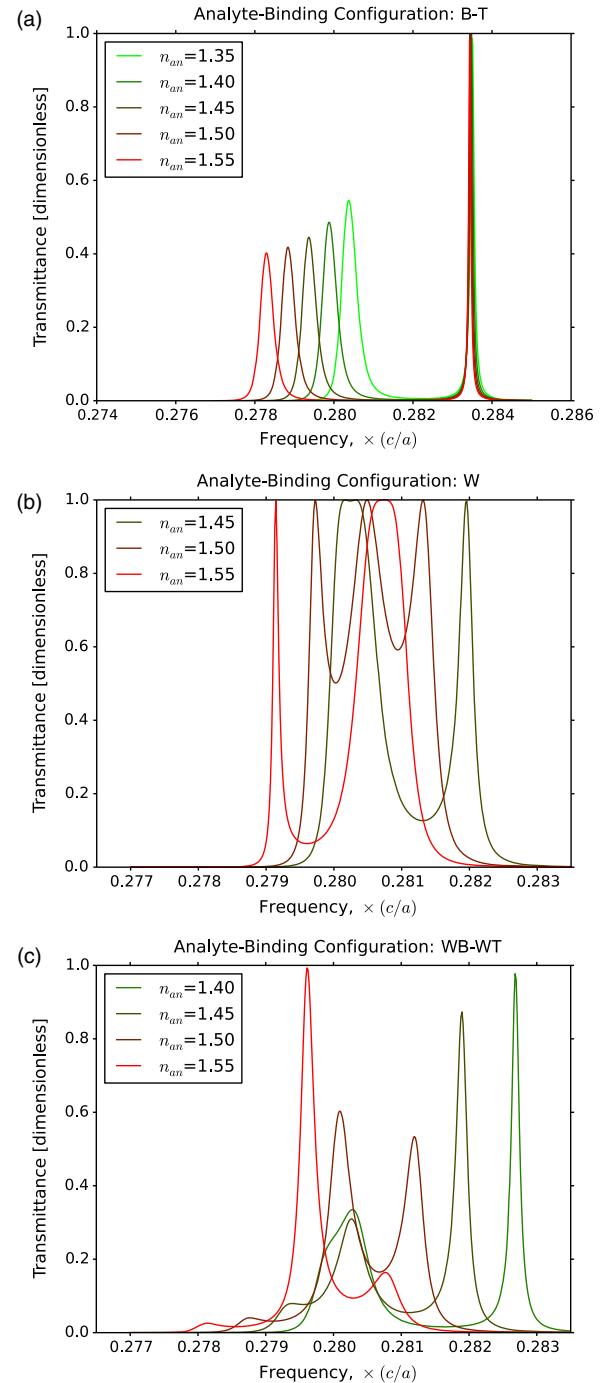


FIG. 13. Transmission spectra for analyte binding with a variable refractive index at $t/a = 0.01$. (a) BT: A higher index is similar to a thicker layer in the spectral signature. (b) W: Two peaks become three, but only for a specific refractive index. (c) WB-WT: Deviation from regular two-peak behavior for $n_{\text{an}} = 1.50$.

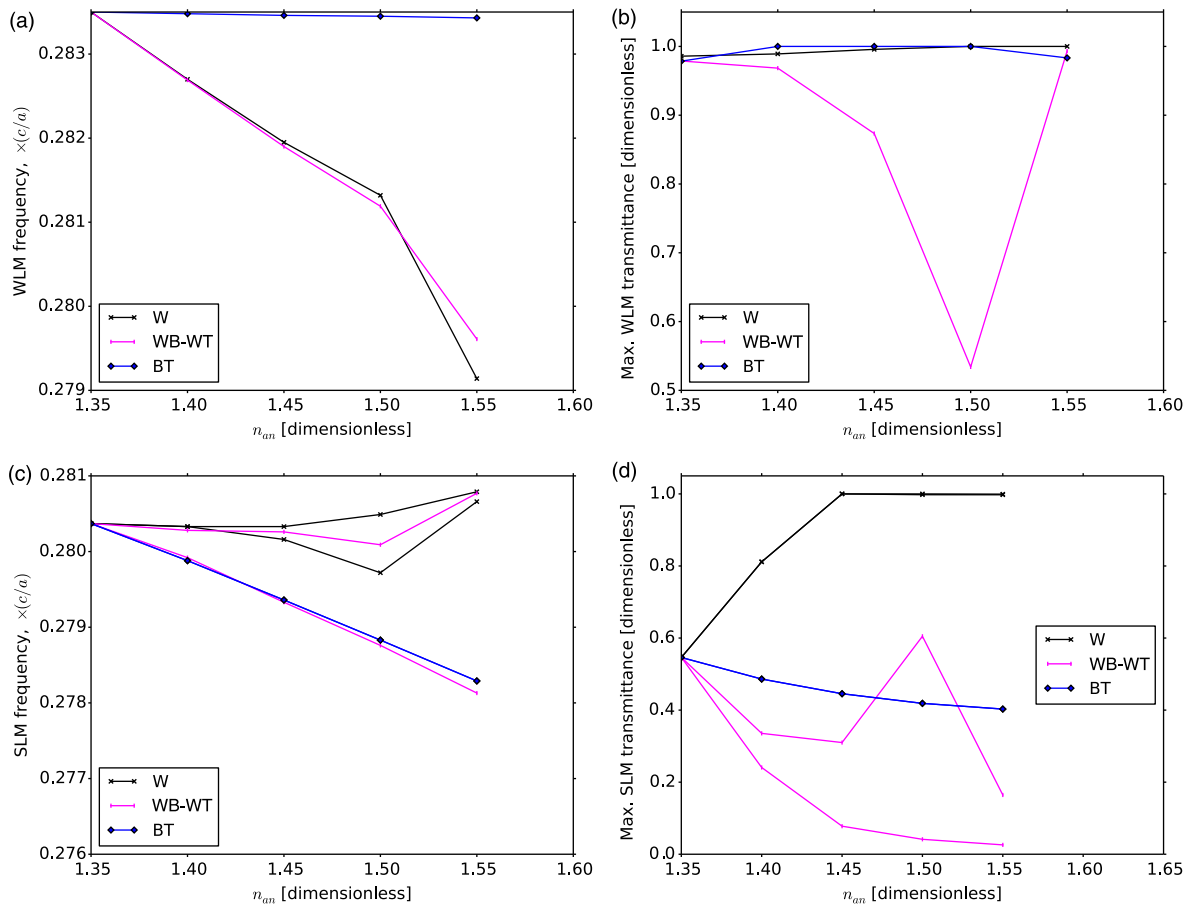


FIG. 14. Summary of sensor response to analyte refractive index variation at $t/a = 0.01$. (a) WLM frequencies: Binding at W is necessary for shifts. (b) WLM peak transmission: Non-negligible changes are seen, unlike t variation at $n_{an} = 1.45$. The WB-WT case exhibits a cusp for $n_{an} = 1.50$. (c) SLM frequencies: Peak splitting occurs for B-T, WB-WT, and even W. (d) SLM peak transmission: Enhancements and suppressions are essentially as seen for t variation at $n_{an} = 1.45$, but the WB-WT case presents an anomalous cusp for $n_{an} = 1.50$.

We plot the sensitivity curves for the WLM and SLM positions and peak transmission levels in Fig. 14. The new mode hybridizations at $n_{an} = 1.50$ appear in the form of sharp cusps in the plots for the W and WB-WT cases.

[1] Valeri Pavlov, Yi Xiao, Bella Shlyahovsky, and Itamar Willner, Aptamer-functionalized Au nanoparticles for the amplified optical detection of thrombin, *J. Am. Chem. Soc.* **126**, 11768 (2004).
 [2] Eli Yablonovitch, Inhibited Spontaneous Emission in Solid-State Physics and Electronics, *Phys. Rev. Lett.* **58**, 2059 (1987).
 [3] Sajeev John, Strong Localization of Photons in Certain Disordered Dielectric Superlattices, *Phys. Rev. Lett.* **58**, 2486 (1987).
 [4] Joshua N. Winn, Robert D. Meade, and J. D. Joannopoulos, Two-dimensional photonic band-gap materials, *J. Mod. Opt.* **41**, 257 (1994).
 [5] Robert D. Meade, Karl D. Brommer, Andrew M. Rappe, and J. D. Joannopoulos, Electromagnetic Bloch waves at the

surface of a photonic crystal, *Phys. Rev. B* **44**, 10961 (1991).
 [6] Mindy R. Lee and Philippe M. Fauchet, Two-dimensional silicon photonic crystal based biosensing platform for protein detection, *Opt. Express* **15**, 4530 (2007).
 [7] John D. Joannopoulos, Steven G. Johnson, Joshua N. Winn, and Robert D. Meade, *Photonic Crystals: Molding the Flow of Light* (Princeton University, Princeton, NJ, 2011).
 [8] E. Chow, A. Grot, L. W. Mirkarimi, M. Sigalas, and G. Girolami, Ultracompact biochemical sensor built with two-dimensional photoniccrystal microcavity, *Opt. Lett.* **29**, 1093 (2004).
 [9] Nina Skivesen, Amélie Têtu, Martin Kristensen, Jørgen Kjems, Lars H. Frandsen, and Peter I. Borel, Photonic-crystal waveguide biosensor, *Opt. Express* **15**, 3169 (2007).
 [10] Valery N. Konopsky and Elena V. Alieva, Photonic crystal surface waves for optical biosensors, *Anal. Chem.* **79**, 4729 (2007).
 [11] Mohamed El Beheiry, Victor Liu, Shanhui Fan, and Ofer Levi, Sensitivity enhancement in photonic crystal slab biosensors, *Opt. Express* **18**, 22702 (2010).

- [12] Jiří Homola, Sinclair S. Yee, and Günter Gauglitz, Surface plasmon resonance sensors: Review, *Sens. Actuators B* **54**, 3 (1999).
- [13] Brian T. Cunningham, Peter Li, Stephen Schulz, Bo Lin, Cheryl Baird, John Gerstenmaier, Christine Genick, Frank Wang, Eric Fine, and Lance Laing, Label-free assays on the BIND system, *J. Biomol. Screening* **9**, 481 (2004).
- [14] J. Vörös, J. J. Ramsden, G. Csucs, I. Szendrő, S. M. De Paul, M. Textor, and N. D. Spencer, Optical grating coupler biosensors, *Biomaterials* **23**, 3699 (2002).
- [15] Ye Fang, Label-free cell-based assays with optical biosensors in drug discovery, *Assay Drug Dev. Technol.* **4**, 583 (2006).
- [16] Ye Fang, Ann M. Ferrie, Norman H. Fontaine, John Mauro, and Jitendra Balakrishnan, Resonant waveguide grating biosensor for living cell sensing, *Biophys. J.* **91**, 1925 (2006).
- [17] Niels Asger Mortensen, Sanshui Xiao, and Jesper Pedersen, Liquid-infiltrated photonic crystals: Enhanced light-matter interactions for lab-on-a-chip applications, *Microfluid. Nanofluid.* **4**, 117 (2008).
- [18] Michael Liss, Birgit Petersen, Hans Wolf, and Elke Prohaska, An aptamer-based quartz crystal protein biosensor, *Anal. Chem.* **74**, 4488 (2002).
- [19] Min Huang, Ahmet Ali Yanik, Tsung-Yao Chang, and Hatice Altug, Sub-wavelength nanofluidics in photonic crystal sensors, *Opt. Express* **17**, 24224 (2009).
- [20] Mark L. Adams, Marko Loncar, Axel Scherer, and Yueming Qiu, Microfluidic integration of porous photonic crystal nanolasers for chemical sensing, *IEEE J. Sel. Areas Commun.* **23**, 1348 (2005).
- [21] Steven Johnson and John Joannopoulos, Block-iterative frequency-domain methods for Maxwell's equations in a planewave basis, *Opt. Express* **8**, 173 (2001).
- [22] Ardavan F. Oskooi, David Roundy, Mihai Ibanescu, Peter Bermel, J. D. Joannopoulos, and Steven G. Johnson, Meep: A flexible free-software package for electromagnetic simulations by the FDTD method, *Comput. Phys. Commun.* **181**, 687 (2010).
- [23] J. J. Sakurai and J. Napolitano, *Modern Quantum Mechanics* (Addison-Wesley, New York, 2011).
- [24] Leo L. Chan, Brian T. Cunningham, Peter Y. Li, and Derek Puff, A self-referencing method for microplate label-free photonic-crystal biosensors, *IEEE Sens. J.* **6**, 1551 (2006).
- [25] R. Schilling, D. Aydin, and O. Levi, in *Proceedings of the Conference on Lasers and Electro-Optics (CLEO), 2012* (IEEE, San Jose, CA, 2012), pp. 1–2.
- [26] Kin Ming Ho, C. T. Chan, C. M. Soukoulis, R. Biswas, and M. Sigalas, Photonic band gaps in three dimensions: New layer-by-layer periodic structures, *Solid State Commun.* **89**, 413 (1994).
- [27] Kenji Ishizaki and Susumu Noda, Manipulation of photons at the surface of three-dimensional photonic crystals, *Nature (London)* **460**, 367 (2009).
- [28] Shawn-Yu Lin, J. G. Fleming, and E. Chow, Two- and three-dimensional photonic crystals built with VLSI tools, *MRS Bull.* **26**, 627 (2001).
- [29] Steven G. Johnson, M. Ibanescu, M. A. Skorobogatiy, O. Weisberg, J. D. Joannopoulos, and Y. Fink, Perturbation theory for Maxwell's equations with shifting material boundaries, *Phys. Rev. E* **65**, 066611 (2002).